

# Study of the extended radio emission of two supernova remnants and four planetary nebulae associated to MIPS GAL bubbles

A. Ingallinera<sup>1,2\*</sup>, C. Trigilio<sup>2</sup>, G. Umama<sup>2</sup>, P. Leto<sup>2</sup>, C. Agliozzo<sup>3,4</sup>, C. Buemi<sup>2</sup>

<sup>1</sup>Università di Catania, Dipartimento di Fisica e Astronomia, Via Santa Sofia, 64, 95123 Catania, Italy

<sup>2</sup>INAF-Osservatorio Astrofisico di Catania, Via Santa Sofia 78, 95123 Catania, Italy

<sup>3</sup>Millennium Institute of Astrophysics, Santiago, Chile

<sup>4</sup>Universidad Andrés Bello, Avda. República 252, Santiago, Chile

Accepted 2014 October 2. Received 2014 September 19; in original form 2014 August 4

## ABSTRACT

We present radio observations of two supernova remnants and four planetary nebulae with the Very Large Array and the Green Bank Telescope. These objects are part of a larger sample of radio sources, discussed in a previous paper, counterpart of the MIPS GAL 24- $\mu\text{m}$  compact bubbles. For the two supernova remnants we combined the interferometric observations with single-dish data to obtain both a high resolution and a good sensitivity to extended structures. We discuss in detail the entire combination procedure adopted and the reliability of the resulting maps. For one supernova remnant we pose a more stringent upper limit for the flux density of its undetected pulsar, and we also show prominent spectral index spatial variations, probably due to inhomogeneities in the magnetic field and in its ejecta or to an interaction between the supernova shock and molecular clouds. We eventually use the 5-GHz maps of the four planetary nebulae to estimate their distance and their ionized mass.

**Key words:** techniques: image processing – planetary nebulae: general – ISM: supernova remnants.

## 1 INTRODUCTION

From the visual inspection of the MIPS GAL Legacy Survey (Carey et al. 2009) mosaic images, obtained with MIPS<sup>1</sup> (Rieke et al. 2004) on board of the *Spitzer Space Telescope*, Mizuno et al. (2010) identified at 24  $\mu\text{m}$  428 compact roundish objects presenting diffuse emission. These small ( $\lesssim 1'$ ) rings, disks or shells (hereafter denoted as ‘bubbles’) are pervasive throughout the entire Galactic plane in the mid-infrared (IR). The main hypothesis about the nature of the bubbles is that they are different type of evolved stars (planetary nebulae, supernova remnants, Wolf–Rayet stars, asymptotic giant branch stars, etc.). However, currently, only about 30 per cent of the bubbles are classified.

In order to shed light on the nature of the bubbles, we had carried out radio continuum observations with the Karl G. Jansky Very Large Array (VLA) in 2010 (C band, configuration D) and 2012 (L band, configuration C and CnB), on a subset of 55 bubbles (Ingallinera et al. 2014; ‘Paper I’ hereafter). We were able to calculate the radio spectral index for 31 of them, finding that at least the 70 per cent are radio thermal emitters. Among the 55 bubbles observed at 5 GHz, ten were classified and, mostly, well known objects. We had excluded these objects from the remainder of that work, mainly aimed at characterising unclassified objects.

In this paper we present an analysis of the VLA radio continuum observations described in Paper I for six of these ten classified bubbles, namely two supernova remnants (SNRs) and four planetary nebulae (PNe), addressed to improve the knowledge of their physical properties. For the two SNRs, whose extension is  $\sim 4$  arcmin, we also conducted single-dish observations with the Green Bank Telescope (GBT). The purpose of these observations was to complement VLA maps with the low spatial frequency information provided by the GBT, to achieve both a high resolution and a high reliability in flux density determination. Also two PNe ( $\sim 1$  arcmin) were observed with the GBT to check if undetected extended emission existed and what kind of improvement, if any, the single-dish data would have brought to VLA maps in this case. The GBT data reduction process and the combination method will be discussed thoroughly, since, by now, no unanimously-accepted standard procedures exist.

## 2 OBSERVATIONS AND DATA REDUCTION

### 2.1 Interferometric observations and data reduction

The interferometric observations and the following data reduction were described in detail in Paper I. Therefore here we will limit to a brief summary.

From the original list of the 428 MIPS GAL bubbles we selected only sources visible at the VLA latitude and with a possible

\* E-mail: ingallinera@oact.inaf.it

<sup>1</sup> The Multiband Imaging Photometer for Spitzer.

detection in NVSS<sup>2</sup> or in MAGPIS<sup>3</sup>. The final subset consisted of 55 bubbles, that were observed at 5 GHz (*C* band) in March 2010 with the VLA in configuration D. Among these 55 bubbles, 40 were subsequently observed at 1.4 GHz (*L* band) in March and May 2012 in configuration C and CnB. For *C*-band observations, each bubble was observed for slightly less than 10 minutes with a total bandwidth of 256 MHz. The average synthetic beam size was around  $25 \times 15$  arcsec<sup>2</sup> and the typical map rms  $\sim 100$   $\mu$ Jy/beam. For *L*-band observations, each bubble was observed for 10 to 20 minutes with a total bandwidth of 1 GHz. The average beam size was  $18 \times 12$  arcsec<sup>2</sup>. The presence of conspicuous radio-frequency interferences limited the sensitivity reached in these observations, and the typical map rms was about 0.5 – 1 mJy/beam.

The entire data reduction process was performed using the package CASA<sup>4</sup>. For all the observations, the bandpass and flux calibrator was 3C286, while for gain calibration, we used a variety of standard calibrators, depending on their distance from the sources (typically within 10°).

Differently from Paper I, the imaging procedure involved the use of the ‘multi-scale algorithm’ (Cornwell 2008). While the standard Clark implementation (Clark 1980) of the CLEAN algorithm (Högbom 1974) assumes that the sky is a collection of point sources on an empty background, the multi-scale CLEAN permits the presence of sources of many different sizes and scales. This algorithm is therefore extremely useful when an extended source is to be imaged. In particular we defined three different scales for source extensions: 0 pixel to search for point sources (equivalent to a normal CLEAN and necessary to properly consider nearby point sources), 5 pixels (about the beam dimension) and 15 pixels.

In Table 2.1 we list all the sources studied in this paper, indicating their main designation, the Mizuno et al. (2010) name ([MGE]) and whether we observed them with the VLA and with the GBT.

## 2.2 Missing low spatial frequencies

An interferometer is an instrument capable to measure the visibility function  $V(u, v)$  that, under certain circumstances, is the Fourier transform of the true sky brightness (e.g. Clark 1999). However, the instrument is able to measure  $V(u, v)$  only on a discrete set of  $(u, v)$  pairs, given by the interferometer baseline projections on the  $uv$  plane. Even if the Earth rotation is exploited, the  $uv$  plane coverage will be always incomplete. In particular there will be a minimum value for  $\sqrt{u^2 + v^2}$  below which no data can be acquired. This minimum value is the projection of the interferometer shortest baseline, and the corresponding angular extension in the real plane is called the ‘largest angular scale’ (LAS).

The impossibility to measure the visibility function at small distances from the  $uv$  plane origin has important consequences in the data imaging. The lack of data in this region of the  $uv$  plane translates to a poor interferometer sensitivity to extended sources. There is no a net extension limit between sources that can be well imaged by interferometer and source that cannot be. We can safely state that only sources with angular dimension significantly smaller than the LAS can be reliably imaged by the interferometer, and that the more extended a source is the more poorly will be imaged.

The imaging artefacts produced by the missing low spatial frequencies prevent the total flux density recovery of the observed source. Therefore this issue, known as the ‘short-spacing problem’ or the ‘flux-loss problem’, prevents also a reliable reconstruction of the source spectral energy distribution.

## 2.3 Single-dish observations and data reduction

In order to fill in the gap in the central zone of the  $uv$  plane and to cross-calibrate the single-dish and interferometer data, we needed to use a single-dish telescope whose diameter was much greater than the VLA minimum baseline, equal to 35 m both in configuration C and D. For this reason we chose to observe with the GBT, which has an effective diameter of 100 m.

The observations were carried out in June 2011 at 1475 MHz (*L* band) and at 5100 MHz (*C* band), with both the receivers collocated in the Gregorian focus of the GBT. For the *L* band the total bandwidth was 20 MHz, while for the *C* band 80 MHz. As back-end we used the Digital Continuum Receiver.

The observing strategy was to map a sky region slightly wider than the VLA field of view. The GBT is equipped with a single-feed receiver but a map can be still obtained by letting the telescope move and scan the desired sky region. In particular we used the ‘on-the-fly mapping’ technique: in this mode, the telescope is slewed within a rectangular area of the sky while it acquires the data and the map is built piling linear scans. Paying attention that, given the telescope beam, an appropriate sampling is made for each scan and that two adjacent linear scans are taken sufficiently close to each other, then the Nyquist sampling theorem guarantees that a reliable map of the sky can be obtained in the limits of instrumental errors. In order to reduce background and instrumental fluctuations, we set a slewing velocity high enough to execute scans of 0.3 s per beam (whose width was chosen to be 3 pixels). This allowed us to reach the desired sensitivity of 5 mJy beam<sup>-1</sup> in *C* band and to observe at the confusion level ( $\sim 20$  mJy beam<sup>-1</sup>) in *L* band. The map dimensions are  $25 \times 25$  arcmin<sup>2</sup> for the *C* band and  $75 \times 75$  arcmin<sup>2</sup> for the *L* band. The scan separation is 50 arcsec for *C* band and 150 arcsec for *L* band, with the expected beam FWHM respectively 2.6 arcmin and 9 arcmin.

The ‘piled-scans’ mapping technique produces an important image artefact, with the resulting map affected by ‘stripes’. A method for stripe removal will be thoroughly discussed in Section 3.1 and in Appendix A1. This method requires that each field is mapped using two different and independent scan directions. We therefore mapped each field using two orthogonal complete scan series along right ascension and declination (see Figure 1). This procedure was repeated twice for each target source.

The entire data reduction process was performed using both routines provided by GBT staff and also by means of routines written by ourselves. First, the raw data from the telescope were converted to the SDFITS format, a particular, non-standard, FITS format explicitly designed to contain single-dish data in binary tables. On these files a flux calibration has been performed. Unavoidable telescope pointing errors did not allow the data acquisition positions to lie on the theoretical points planned and instructed to the telescope. We used interpolation via triangulation to regrid the data to the desired pattern (see Appendix A2). The calibrated and re-gridded data were eventually used to create a standard FITS image.

<sup>2</sup> <http://www.cv.nrao.edu/nvss/NVSSlist.shtml> (Condon et al. 1998).

<sup>3</sup> <http://third.ucllnl.org/gps/catalogs.html> (Helfand et al. 2006).

<sup>4</sup> <http://casa.nrao.edu> (McMullin et al. 2007).

Designation	[MGE]	Right ascension (J2000)	Declination (J2000)	Observations		
				VLA 5GHz	VLA 1.4GHz	GBT
SNR G011.2-00.3	011.1805-00.3471	18:11:28.9	-19° 25' 29''	yes	no	yes
SNR G027.4+00.0	027.3891-00.0079	18:41:19.9	-04° 56' 06''	yes	yes	yes
PN G029.0+00.4	029.0784+00.4545	18:42:46.8	-03° 13' 17''	yes	yes	yes
NGC 6842	065.9141+00.5966	19:55:02.4	+29° 17' 20''	yes	no	yes
PN G040.3-00.4	040.3704-00.4750	19:06:45.8	+06° 23' 53''	yes	yes	no
PN G031.9-00.3	031.9075-00.3087	18:50:40.1	-01° 03' 09''	yes	yes	no

**Table 1.** List of the sources studied in this work.

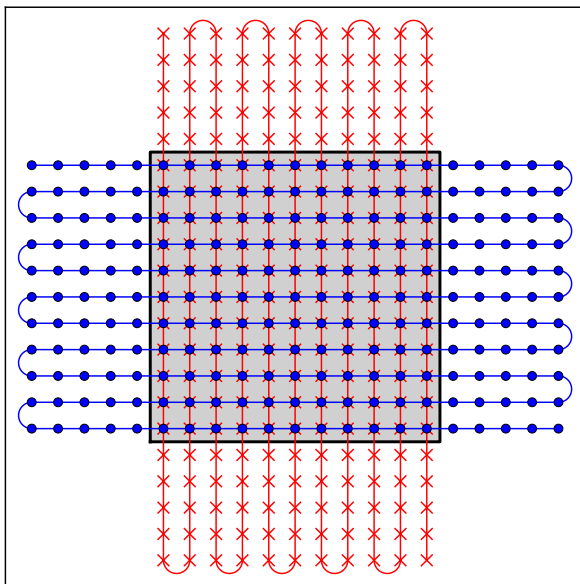


**Figure 1.** A schematic illustration of the two intersecting scan series used in this work. The shadowed area is the sky region to map; first the telescope is moved along the horizontal path, with a data acquisition at each circle, then the piled scans are performed in the orthogonal direction, following the vertical path (crosses represent acquisition points).

### 3 COMBINING GBT AND VLA MAPS

#### 3.1 Destriping single-dish maps

The map construction method described in Section 2.3 produces important artefacts in the final image. In particular, instrumental drifts during mapping time usually give rise to a different baselevel for each scan and the resulting image appears affected by ‘stripes’, running in the same direction of the scans. The simplest way to take into account these baselevel drifts is to estimate their contribution in a region supposed to be free of emission. This can be obtained by letting the scans be more extended than the region to map and then using these extra-points, at both side of the map area, to linearly fit a baselevel that will be subtracted from each scan. In many circumstances, however, this method may not give a satisfactory result. Emerson & Gräve (1988) (EG88) pointed out three main limitations: first, there can be emission at the end of each scan; second, also the scan ends are affected by noise which can have great effects on the baseline determination; third, it is possible that a baseline cannot be adequately represented by a linear fit. In their paper, they discussed the general problem of the reduction

of scanning noise in raster scanned data, with no limitations to the single-dish single-feed radio telescope case presented above. The solution proposed by EG88 was to filter out the spatial frequencies responsible for stripes by means of opportune weights to the data in the Fourier domain.

One of the most important problems when one maps a portion of the sky in the Galactic plane, with the resolution of the GBT, is that there are no large regions free of emission in the neighbourhood of any source. Therefore it is mandatory to use a destriping algorithm such as the one by EG88, since no reliable baselevel estimation at the ends of the scan can be made. However the strategy to create the maps with scans extended only few arcminutes with the telescope scanning quickly gives us two important advantages: the systematic errors along each scan can be considered constant and the small amount of pixels constituting the map allows to work more surgically in the Fourier plane. Therefore we modified the EG88 algorithm to better fit our problem. A detailed description of the adopted solution is reported in appendix A1.

The main advantage of this method, compared to the EG88 algorithm, is the preservation of the information from all spatial frequencies. In particular the central pixel in the Fourier plane maintains its value. This is very important because, as we said, its value is the sum of all pixel values and therefore if it were (almost) zero several negative-valued features would appear in the destriped image. Even if in the real image it accounts only for a flat base level (i.e. even a zero central pixel in the Fourier plane does not introduce further artefacts), it may play a role in the combination process. The preservation of the central pixel in the Fourier plane guarantees the map total flux density is conserved after the destriping procedure. However this could be not true for a single source. We tested this possible flux density alteration comparing sources from pre- and post-destriped maps (for details see Appendix A2). We found that the error introduced by the destriping process is negligible with respect to the other source of error discussed in this work (like calibration errors or background noise).

#### 3.2 Map combination

As discussed, one of the goal of this work is to combine interferometric and single-dish maps. However, despite the presence of several works regarding the flux-loss problem and the combination of interferometric and single-dish data, only a few reliable implementations of the theoretical algorithms found in literature were available. Our choice was to use the new CASA tool, CASAFEATHER, introduced in version 4.1.

The theory behind the combination we aimed to perform is rather simple. It is based on the fact that a single-dish telescope measures not only a single spatial frequency, but a whole range of continuous spatial frequencies up to a maximum one, which cor-

responds to the diameter of the dish,  $D$ . Hence, a single-dish telescope behaves as an interferometer with a continuous range of baselines, from zero to  $D$ . The Fourier transform of a single-dish image is a two-variable complex function that can be interpreted as the ‘intensity’ of each bidimensional spatial frequency. On the other hand, an interferometer directly observes the source in the Fourier domain, measuring the visibility function, but it is not able to fill the entire Fourier plane, and in particular it will not cover the inner region of this plane up to a spatial frequency corresponding to the shortest baseline. This ‘hole’ is usually filled during the imaging process through some kind of interpolation, which, however, cannot provide reliable values for the missing visibility (more precisely it should be treated as an extrapolation).

If the single-dish telescope diameter is greater than the shortest baseline of the interferometer, there would be an annular region in the Fourier plane inside which we have both interferometric and single-dish data for the source, i.e. the single-dish and the interferometer are sensitive to the emission related to some common spatial frequencies. The trick now is to use this overlapping region in the Fourier plane to cross-calibrate the data and make them as coincident as possible in this region. This operation is known as ‘feathering’. The CASAFEATHER tool allows the user to control some parameters involved in the feathering process. In particular we set the effective dish diameter to 80m and single-dish image scaling factor from 1 to 2.5. We can then merge the two datasets to obtain a single visibility function defined from the zero baseline to the longest interferometer baseline. An inverse transformation of the visibility obtained in this way results in an image with the same resolution of the original interferometric image, but also with well determined low spatial frequencies. From this combined image a total flux density recovery is possible. It is hard to determine the reliability of this measurement. We found however that the flux densities should be corrected within 5 or 10 per cent, depending on the particular map (see Appendix A2).

The actual result of the combination varied appreciably for the different sources. For the two SNRs the combined maps show a significant improvement in terms of image quality as well as an increasing in total flux density. In particular the recovered extended emission is now clearly spatially coincident with the diffuse emission present in the MIPSGAL images. In the GBT images, both the two SNRs are characterised by a high total flux density at 5GHz ( $> 1$  Jy for both), are (among) the brightest sources in their neighbourhood and are clearly (at least at 5GHz) detached by other extended sources. These three properties proved to be extremely important in the combination process, triggering between a useful combination and a disappointing result. All the other sources are less extended than the two SNRs. In these cases the GBT maps allowed us to exclude the presence of diffuse emission around these sources, reassuring that the VLA flux density estimates can be considered reliable.

## 4 DISCUSSION

We discuss now on the results obtained for the two SNRs and the four PNe. We report a very brief summary of state-of-art knowledge for each one of them. We present then our maps and derive from them different physical parameters that complement or improve the values available in literature.

### 4.1 SNR G011.2-00.3

The SNR G011.2-00.3 is a well studied radio, IR and X-ray source. Very likely, it is the remnant of the historical SN 386 (Reynolds et al. 1994). The radio emission associated to this object has been first detected at 2.7 and 5 GHz by Altenhoff et al. (1970) and at 408 MHz by Shaver & Goss (1970). It was proposed as a SNR by Dickel & Milne (1972) from the lack of the H109 $\alpha$  line. The source was subsequently observed in a wide range of radio frequencies, from 30.9 MHz to 32 GHz (Becker & Kundu 1975; Milne 1979; Downes 1984; Morsi & Reich 1987; Kassim 1988). In particular the 32-GHz observations by Morsi & Reich (1987) revealed a deviation from the spectral index calculated at the lower frequencies, interpreted as the evidence of a composite-type SNR (Vasisht et al. 1996). This implied also the presence of a central pulsar, discovered by Torii et al. (1997) with a period of 65 ms and with a possible accretion disk (Glushak 2014). The remnant is thought to have originated from a IIL/b SN (Koo et al. 2007) and an early-B type progenitor (Kothes & Reich 2001).

In Figure 2 we report the GBT images obtained respectively at 1.4 GHz and 5 GHz after the destriping procedure described in Section 3.1. At 1.4 GHz the source is not resolved but appears quite far from nearby objects so that background estimation is not hard. At 5 GHz the GBT beam is small enough to resolve the SNR (the other radio sources detected at 1.4 GHz are not visible because they are out of boundary). However it is possible to notice a point source just below the SNR, too close to allow the huge beam at 1.4 GHz to resolve the two distinct objects. In this case a flux density measurement at 1.4 GHz only on GBT map could be overestimated.

We produced a high resolution map at 5 GHz combining the GBT data and the VLA map as described in Section 3.2. The resulting image is shown in Figure 3. The composite-type nature of the SNR is evident, with a prominent shell and a perfectly recognisable pulsar wind nebula (PWN) at its center. We calculated a flux density of  $8.2 \pm 0.8$  Jy, in agreement with previous determination (Downes 1984). In contrast, the flux density determined only on the VLA data was about 3 Jy, showing an important flux loss. It is extremely important to notice that our flux density determination derives from the combination of single-dish and interferometer data, and the fact that its value agrees with single-dish estimates from literature strongly corroborates the entire data reduction process. This excellent reliability is fundamental for more quantitative analysis, as the one presented in the next section for the other SNR.

### 4.2 SNR G027.4+00.0

The radio emission associated to SNR G027.4+00.0, also known as KES 73, is located in a particularly crowded region. At radio wavelengths, the entire region was first detected as a single discrete source at 408 MHz (Large, Mathewson & Haslam 1961). Higher resolution images at 5 GHz resolved the huge radio emission region in at least four discrete components. One of them presented a clearly non-thermal emission and was proposed as a SNR (Milne 1969; Angerhofer, Becker & Kundu 1977).

Kriss et al. (1985) gave the first evidence that the SNR harboured a compact source, by means of X-ray observations. This compact source, designed 1E 1841-045, is an anomalous X-ray pulsar with a period of 11.8 s (Vasisht & Gotthelf 1997). It is characterised by an extremely intense magnetic field (Gotthelf, Vasisht & Dotani 1999) and shows soft  $\gamma$ -ray repeater like bursts (Kumar & Safi-Harb 2010; Lin et al. 2011). It is now an established magnetar (Kumar et al. 2014).

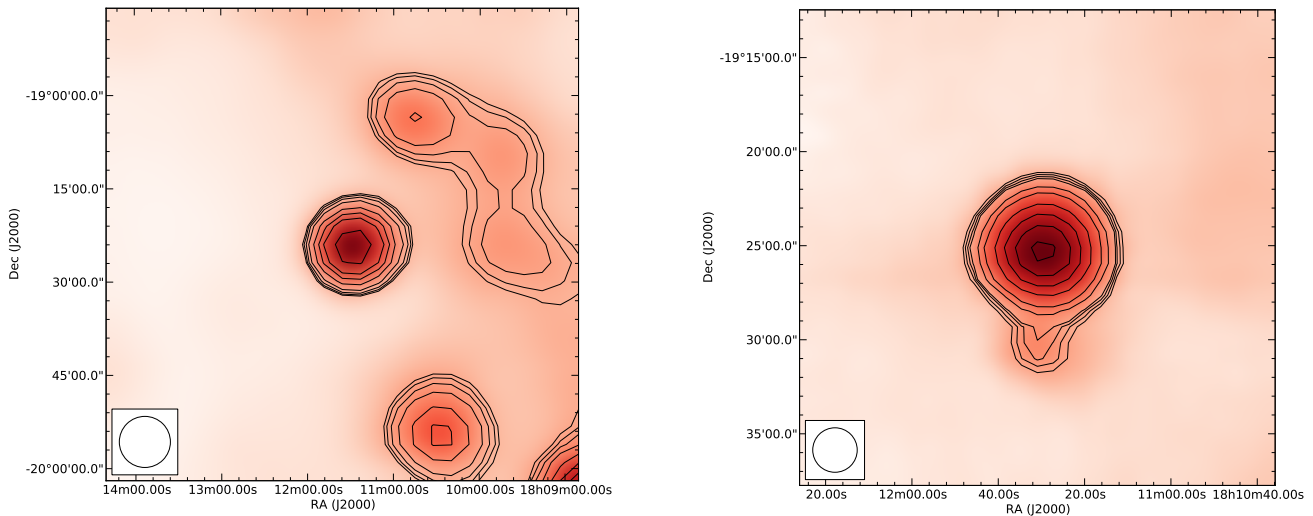


**Figure 2.** GBT images of SNR G011.2-00.3 at 1.4 GHz (left) and 5 GHz (right). At 1.4 GHz the source appears point-like and well distant from other sources. At 5 GHz the source is resolved and another background source is clearly detected below the SNR. Please note that the scale of the two images is different.

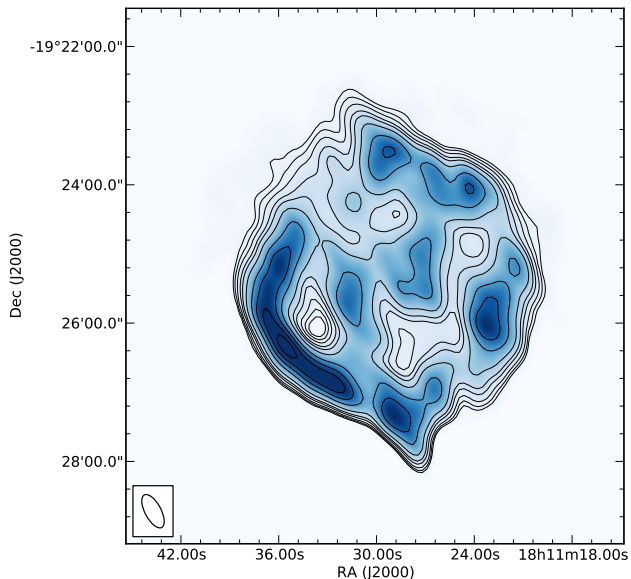


**Figure 3.** High resolution images of SNR G011.2-00.3 at 5 GHz. The image is the result of feathering VLA (configuration D) and the GBT map.

Studies on H I absorption line toward the source pose the SNR at a distance of about 7.5 kpc (Sanbonmatsu & Helfand 1992; Tian & Leahy 2008). The nebula originated  $\lesssim 2000$  yr ago from a core collapsing SN (type II or Ib) and a progenitor mass  $\gtrsim 20M_{\odot}$  (Gottlieb & Vasishth 1997; Tian & Leahy 2008; Kumar et al. 2014).

In Figure 4 we report the GBT images we obtained respectively at 1.4 GHz and 5 GHz. It is possible to notice how the radio emission from the surrounding sources discussed above is clearly detected. At 5 GHz the GBT is able to easily resolve the SNR from the remainder of radio sources while at 1.4 GHz the SNR is not totally detached.

A high resolution map at 1.4 GHz has been created using VLA data from both our observations (configuration C; Section 2.1) and archive data (configuration B), and combining them via

CASA FEATHER. Though the source is less extended than the VLA LAS at this frequency we further combined this high resolution image with the GBT map. The result is shown in Figure 5 (left). The calculation of the total flux density of the SNR proved hard because of the peculiar background. We measured a value of  $5.5 \pm 0.8$  Jy, compatible with the value in literature (Koo & Heiles 1991). There is no evidence of radio emission from the pulsar, with a flux density upper limit of 0.33 mJy at  $3\sigma$  level (previous estimates gave an upper limit of 0.60 mJy at this frequency, see Kumar et al. 2014).

At 5 GHz we did not find useful archive observations and we created a high resolution map combining the GBT map and the VLA data (configuration D; Section 2.1). The combined image is shown in Figure 5 (right). In this case the source was more extended than the VLA LAS and the availability of single-dish data proved crucial to recover the total flux density. For this frequency we calculated a flux density of  $2.3 \pm 0.4$  Jy, in accordance with previous estimates (Angerhofer, Becker & Kundu 1977; Caswell et al. 1982). For comparison, the flux density computed only on the VLA map was  $0.51 \pm 0.01$  Jy, and therefore, in this case, we can see a flux-loss of at least a factor 4.

Given the flux densities computed above we can derive a global spectral index  $\alpha = -0.70 \pm 0.18$ , in perfect agreement with previous estimates in other spectral region (the turnover is around 100 MHz; Caswell et al. 1982; Kassim 1989). Starting from the two images presented in Figure 5 we were also able to build a spectral index map. In particular we convolved both the images with an opportune bidimensional Gaussian in order to obtain for both a circular beam of 25 arcsec. The convolved images were subsequently regridded to have a pixel-by-pixel correspondence and the spectral index map was created. The result is shown in Figure 6. Not only a prominent spectral index variation is evident but it is also possible to notice a flatter index toward the pulsar with respect to the global value, as well as an important asymmetry, with the western region flatter than the eastern one. A spectral index of about  $-0.3$  around the pulsar is usually associated to the presence of a PWN (Gaensler & Slane 2006). However this should not be the case since this SNR is classified as a pure shell-type remnant and, furthermore, PWNe surrounding a magnetar have never been detected. The western region appears the brightest one not only in radio but also in IR and

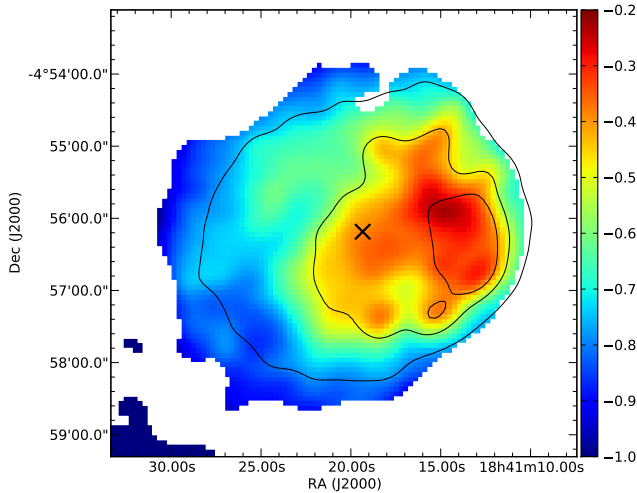


**Figure 6.** Spectral index map of SNR G027.4+00.0. The super-imposed contours refer to the 5-GHz map convolved to a circular 25-arcsec beam (see text). The pulsar is indicated with a black cross.

X-ray and it is characterised by a higher column density with respect to the other regions (Kumar et al. 2014). Being the compact star a magnetar, it is possible to hypothesise that its strong magnetic field has an influence on the western region, increasing the remnant intensity. Moreover, spatial inhomogeneities in the magnetic field intensity lead to variations of the emission turnover. Overlapping synchrotron contributions with different turnover frequencies could finally result in a flatter spectral index. Alternatively, Giacani et al. (2011) discussed a similar picture for the shell-type SNR G344.7-00.1, where a flat spectral index around  $-0.3$  is measured toward the central regions. They notice that in that region there is an important correspondence between the radio and the  $24\text{-}\mu\text{m}$  emission. They conclude that the flatter spectral index derives from the SN shock impacting a dense molecular cloud, resulting in a radiatively energy loss. In Figure 7 we show a superposition of MIPS GAL  $24\text{-}\mu\text{m}$  image of SNR G027.4+00.0 with our radio maps. We can notice that in the western region the IR and the  $1.4\text{-GHz}$  emission are coincident. A morphological comparison between  $24\text{-}\mu\text{m}$  and  $5\text{-GHz}$  image is more difficult because of the poor resolution of the radio map. The  $5\text{-GHz}$  emission seems to trace well the  $24\text{-}\mu\text{m}$  image in the north-west part of the SNR (which is the region with the flattest spectrum) and partially in its centre. A satisfactory morphological analysis would require that also  $5\text{-GHz}$  map had about the same resolution of the IR image. Though the correlation between IR and radio for our SNR appears less stringent than for SNR G344.7-00.1 we cannot rule out the hypothesis of shock impacting dense molecular cloud as a cause of spectral flattening. Finally another limb-flattened spectral index behaviour is reported by Bhatnagar et al. (2011) for the composite-type SNR G016.7+00.1.

### 4.3 Planetary nebulae

One of the main conclusions of Paper I was that the great majority of the MIPS GAL bubbles showing radio emission could be classified as PNe. In that sense, the radio study of these objects had proved an extremely powerful instrument for finding undiscovered PNe (currently only about 10 percent of the expected galactic PNe have been found). However the sole IR and radio images were insufficient to determine many physical characteristics of these PNe

and we could not go further than the mere, sometimes tentative, classification.

In this section we present the PNe in our sample. We derive some physical properties starting from the radio maps, given their electron temperature (see, for example, Wilson, Rohlfs & Huttemeister 2012). For each PN, we consider the  $5\text{-GHz}$  map and we assume that at this frequency the nebula is an optically-thin free-free emitter, as derived from their spectral index (see Table 4.3). Under this assumption the nebula brightness  $B$  is given by

$$B = B_{\text{bb}}(T_e)\tau_\nu, \quad (1)$$

where  $T_e$  is the electron temperature,  $B_{\text{bb}}(T_e)$  is the brightness of a black body at a temperature  $T_e$  and  $\tau_\nu$  is the optical depth at the frequency  $\nu$ . If  $T_e$  is known, from the brightness map it is possible to derive an optical-depth map. The optical depth is related to the emission measure EM through the relation

$$\tau_\nu = 8.235 \times 10^{-2} T_e^{-1.35} \left( \frac{\nu}{\text{GHz}} \right)^{-2.1} \left( \frac{\text{EM}}{\text{pc} \cdot \text{cm}^{-6}} \right). \quad (2)$$

If also the distance is known it is possible to estimate the dimension of the nebula. In this case the electron density  $n_e$  can be derived from the relation

$$\text{EM} = \int_0^s n_e^2 ds, \quad (3)$$

where  $s$  is the line-of-sight coordinate. Assuming an opportune geometry for each PN and that the nebular gas is completely ionized hydrogen, it is finally possible to derive the PN ionized mass as a volume integral:

$$M_{\text{ion}} \approx \int_V n_e m_p dV, \quad (4)$$

where  $m_p$  is the proton mass.

From the equation (4), and considering the previous ones, it is possible to show that

$$M_{\text{ion}} \propto T_e^{0.35} D^{5/2}, \quad (5)$$

where  $D$  is the distance. Therefore, the ionized mass shows only a weak dependence on  $T_e$ , while it is very sensitive to the nebula distance. The distance values from literature usually suffer of important uncertainties. Given the nebula flux density at  $5\text{ GHz}$  and its mean angular radius, we used the formula derived by van de Steene & Zijlstra (1995), which holds only for optically thin sources, to calculate the PN statistical distance. We adopted this value as the best distance estimate, except for the last PN (see Section 4.3.4). The less critical dependence on  $T_e$  allows us to safely assume a typical value of  $10^4\text{ K}$  whenever no previous estimates were available.

In the Table 4.3 we report the mean electron density, the distance and the ionized mass that we derived for the four PNe. A brief discussion on each one of them follows.

#### 4.3.1 PN G029.0+00.4

Also known as Abell 48, PN G029.0+00.4 was first discovered thanks to the National Geographic Society–Palomar Observatory Sky Survey and recognised as PN after its morphology (Abell 1955; Abell 1966). Optical spectroscopy of the central star by Wachter et al. (2010) seemed to dispute its nature of PN in favour of a WR star with a surrounding nebula. However, recently, Todt et al. (2013) and, independently, Frew et al. (2014) (F14 hereafter) conducted extremely deep spectroscopic studies both on the central source

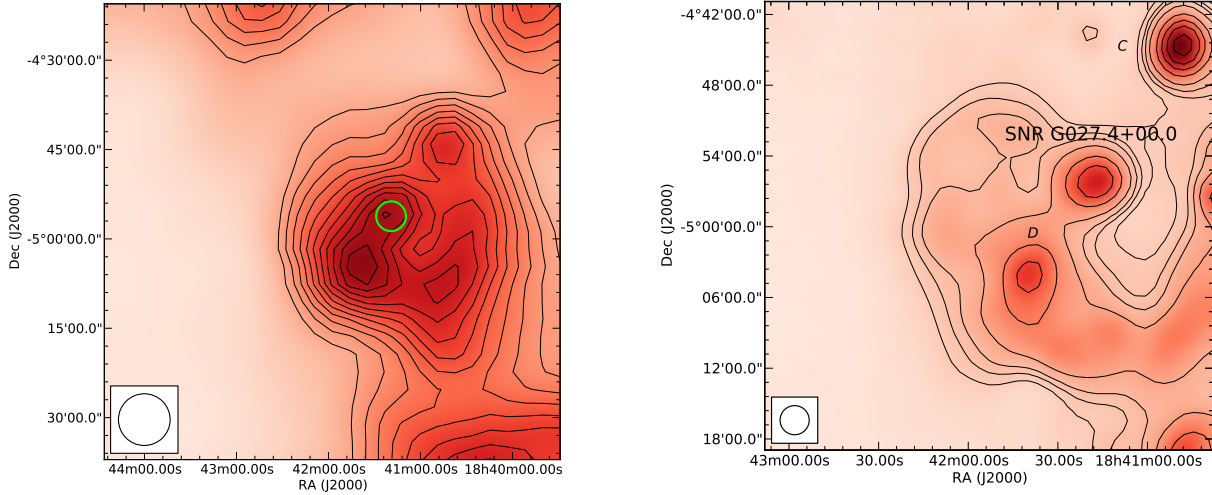


**Figure 4.** GBT images of SNR G027.4+00.0 at 1.4 GHz (left) and 5 GHz (right). At 1.4 GHz our map cover the entire radio emitting region described by Large, Mathewson & Haslam (1961), and the SNR is highlighted with a green circle. At 5 GHz we were able to clearly separate the SNR from the remainder of the other radio sources, as well as resolve the source itself. Labels C and D are as in Angerhofer, Becker & Kundu (1977). Please note that the scale of the two images is different.

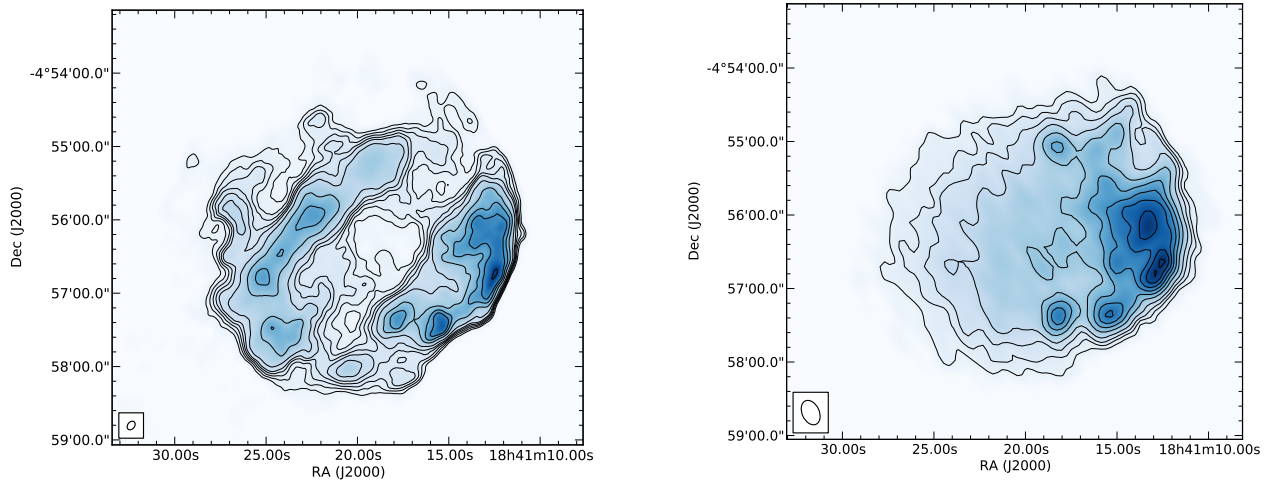


**Figure 5.** High resolution images of SNR G027.4+00.0 at 1.4 GHz (left) and 5 GHz (right). The 1.4 GHz image was obtained combining GBT and VLA B- and C-configuration data. The 5 GHz image is the result of feathering VLA (configuration D) and the GBT map.

Source	$\langle n_e \rangle$ ( $\text{cm}^{-3}$ )	$D$ (kpc)	$T_e$ ( $10^3$ K)	$M_{\text{ion}}$ ( $M_{\odot}$ )	$\alpha$
PN G029.0+00.4	39.2	1.6	7.5	0.1	-0.09
NGC 6842	15.6	2.2	13.2	0.1	
PN G040.3-00.4	29.3	2.1	10.0	0.2	-0.06
PN G031.9-00.3	14.3	3.2	10.0	0.1	0.49

**Table 2.** Physical parameters for the four PNe. The first column is the mean electron density as derived from our 5-GHz map. In the second we report the distance value used to compute the ionized mass. The third column lists the electron temperature as reported in literature for the first two PNe and the assumed value of  $10^4$  K for the other two (see text). In the fourth column we report the ionized mass while in the last one the radio spectral index.

and on the nebula. The two groups came to the same conclusion that Abell 48 is indeed a PN harbouring an extremely rare [WN5] or [WN4-5] star. The distance of PN G029.0+00.4 has been estimated between 1.6 and 1.9 kpc (Cahn & Kaler 1971; Ortiz 2013; Todt et al. 2013; F14).

This object was observed in the IR by *Spitzer* (both IRAC and MIPS), *WISE* and *AKARI* (Phillips & Ramos-Larios 2008; Phillips & Márquez-Lugo 2011). The mid-IR infrared colour, in particular, was used by F14 as one of the indicator of the PN nature. The first radio detection was made by Cahn & Rubin (1974) at 11.1 cm and then in the NVSS at 1.4 GHz (Condon & Kaplan 1998).

Our VLA map at 5 GHz is presented in Figure 8. The source extension ( $\sim 1$  arcmin) is well below the LAS of the VLA in configuration D, therefore a combination with the GBT data proved un-

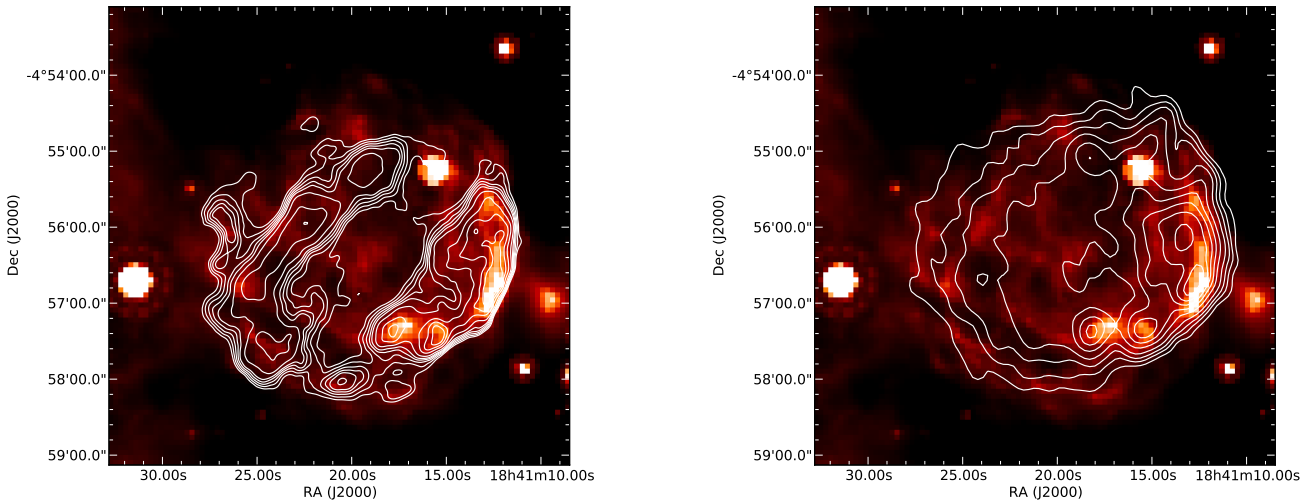


**Figure 7.** Superposition of the MIPSGAL 24- $\mu\text{m}$  image of SNR G027.4+00.0 and radio contours at 1.4 GHz (left) and 5 GHz (right). The images at 24  $\mu\text{m}$  and at 1.4 GHz have approximately the same resolution. We can notice that the western region appears bright both in IR and in radio. The north-west region and the central part of the SNR are those with the flattest spectrum. In these two regions the IR emission seems co-spatial with the 5-GHz one but the poorer resolution of the latter does not permit definitive conclusions. The bright IR source in the north-west region of the SNR is the unrelated star IRAS 18385-0458.

necessary. Indeed a test combination was performed and, as expect, no significant variations were revealed. The resolution achieved in Figure 8 ( $19.5 \times 14 \text{ arcsec}^2$ ) is worse than the resolution of NVSS archive image at 1.4 GHz, however the bipolar structure of the PN is still recognisable. For this source, we estimated a flux density at 5 GHz  $S_C = 142.4 \pm 4.3 \text{ mJy}$ . Using the NVSS flux density value at 1.4 GHz  $S_L = 159 \pm 15 \text{ mJy}$ , we derived a spectral index  $\alpha = -0.09 \pm 0.08$ , in accordance with a optically-thin free-free emission. From the 5-GHz flux density we derived a statistical distance of  $1.6 \pm 0.2 \text{ kpc}$ .

F14 were able to estimate the ionized mass of the nebula exploiting the integrated  $\text{H}\alpha$  flux density. They found  $M_{\text{ion}} \sim 0.3\sqrt{\epsilon}M_{\odot}$ , where  $\epsilon$  is the nebula filling factor. We used the map at 5 GHz to provide a different approach to the same problem. Assuming an electron temperature of 7500 K (F14) and a depth equal to its mean diameter (this assumption holds also for the following PNe), we found  $M_{\text{ion}} \sim 0.12M_{\odot}$ . This value is in agreement with the one from F14 and is compatible with the typical ionized mass values for PNe (Frew & Parker 2010).

#### 4.3.2 NGC 6842

First listed in the New General Catalogue (Dreyer 1888), NGC 6842 was classified as PN by Curtis (1919) because of its morphology. It appears as a ring nebula with a diameter of  $\sim 50 \text{ arcsec}$  (Hromov & Kohomek 1968). Despite the fact that several studies have dealt with its distance determination, to date there is no a strong agreements among the various estimates, with values ranging from 1.25 to 2.9 kpc (O'dell 1962; Cahn & Kaler 1971; Zhang 1995; Gorny, Stasińska & Tylenda 1997; Tajitsu & Tamura 1998; Phillips 2004; Giammanco et al. 2011).

The source has been observed at radio frequencies from 327 MHz to 5 GHz (Taylor & Gregory 1983; Gregory & Taylor 1986; Taylor et al. 1996; Condon & Kaplan 1998), and its nature of thermal emitter has been proven (Taylor et al. 1996).

In Figure 9 we present a 5-GHz map obtained with the VLA in configuration D. So far, it is the second interferometric map at this

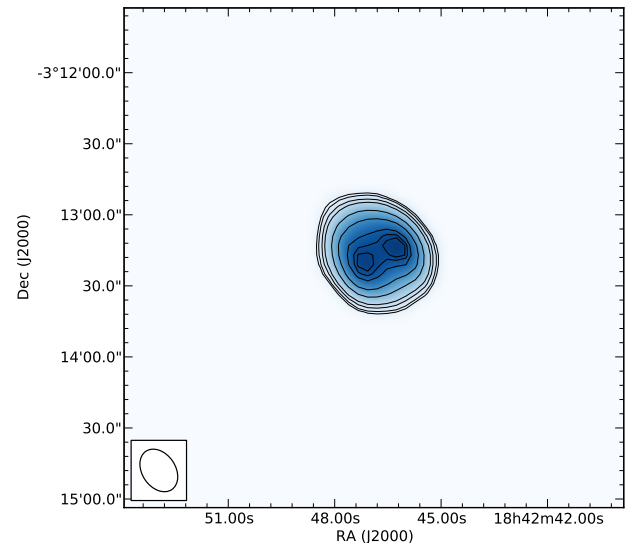


**Figure 8.** VLA image of PN G029.0+00.4 at 5 GHz.

frequency after the one published by Zijlstra, Pottasch & Bignell (1989). The high sensitivity of our map allowed us to determine an accurate flux density of  $37.9 \pm 1.1 \text{ mJy}$ , in good agreement with the single dish estimate of Gregory et al. (1996) of  $39 \pm 5 \text{ mJy}$ . The statistical distance determined from the 5-GHz flux density is  $2.2 \pm 0.3 \text{ kpc}$ .

We used the 5-GHz map to calculate the ionized mass of the nebula. Considering an electron temperature  $T_e = 13 \text{ 200 K}$  after Kaler (1983) the ionized mass of NGC 6842 results of order of  $0.1M_{\odot}$  (with the greatest uncertainties deriving from the distance assumption). Note that Lenzuni, Natta & Panagia (1989) calculated an ionized mass  $M_{\text{ion}} = 0.17M_{\odot}$  and Gorny, Stasińska & Tylenda (1997) for the central star  $M_{\star} \simeq 0.6M_{\odot}$ .



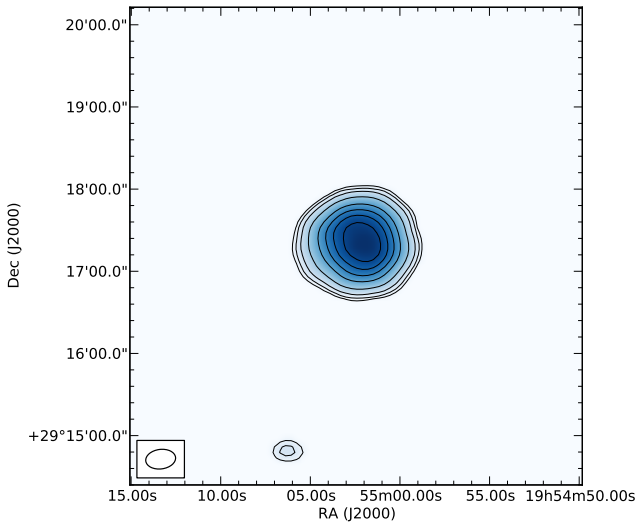


Figure 9. VLA image of NGC 6842 at 5 GHz.

#### 4.3.3 PN G040.3-00.4

PN G040.3-00.4 was first detected and recognised as PN by Abell (1955; 1966). In the optical it appears as a ring nebula with a diameter of about 50 arcsec. Several studies indicate that this PN is located at a distance  $d \sim 2$  kpc, though the various estimates range from 1.6 to 3 kpc (Cahn & Kaler 1971; Kaler 1983; Maciel 1984; Sabbadin 1986; Cahn, Kaler & Stanghellini 1992; Stanghellini, Corradi, & Schwarz 1993; Zhang 1995; Phillips 2004; Ortiz 2013).

The source has been detected at IR wavelengths with *Spitzer* (Phillips & Ramos-Larios 2008; Kwok et al. 2008) and *AKARI* (Phillips & Márquez-Lugo 2011). It was first observed at radio wavelength by Milne & Aller (1982) at 14.7 GHz, then by Condon & Kaplan (1998) at 1.4 GHz (NVSS) and by Pazderska et al. (2009) at 30 GHz.

We observed the source with the VLA both at 1.4 GHz (configuration CnB) and at 5 GHz (configuration D). In Figure 10 we present the two maps. The flux density we computed at 5 GHz is  $S_C = 59.7 \pm 0.5$  mJy while at 1.4 GHz we find  $S_L = 64.1 \pm 0.8$  mJy and a resulting spectral index  $\alpha = -0.06 \pm 0.01$  (see Paper I). It is important to notice that the NVSS catalogue lists a flux density of  $33.6 \pm 1.1$  mJy at 1.4 GHz, significantly lower than our value. A cross check with the VLA Galactic Plane Survey maps (Stil et al. 2006), observed in 2000, revealed a flux density in perfect agreement with our estimate rather than the NVSS one. We conclude that the reported NVSS flux density is very likely incorrect.

From the 5-GHz map we computed a statistical distance of  $2.1 \pm 0.3$  kpc. Assuming an electron temperature  $T_e = 10^4$  K (to our knowledge, there is no real estimate of  $T_e$  in literature), we can calculate an ionized mass  $M_{\text{ion}} \sim 0.2 M_{\odot}$ .

#### 4.3.4 PN G031.9-00.3

Very little is known about PN G031.9-00.3. Discovered and classified by Weinberger & Sabbadin (1981), a tentative distance of 4.7 kpc has been given by Dobrinčić et al. (2008) from Galactic rotation curves. It was detected as radio source at 1.4 GHz in NVSS and by White, Becker & Helfand (2005) at 5 GHz.

In Figure 11 we present the two maps derived from our data.

For this PN we found at 5 GHz a flux density of  $S_C = 19.6 \pm 0.8$  mJy while at 1.4 GHz  $S_L = 10.8 \pm 3.7$  mJy (see Paper I). The resulting spectral index is  $\alpha = 0.49 \pm 0.28$ , showing that the source is still optically thick at 1.4 GHz. The statistical distance computed for this PN is  $3.2 \pm 0.5$  kpc, significantly different from the literature value. It is possible that the distance calculation is biased by the fact that the nebula could be not completely optically thin at 5 GHz as suggested by the spectral index. For this reason we safely report the ionized mass derived from the literature distance and from our estimate. Assuming an electron temperature  $T_e = 10^4$  K, we find  $M_{\text{ion}} \sim 0.3 M_{\odot}$  if  $D = 4.7$  kpc and  $M_{\text{ion}} \sim 0.1 M_{\odot}$  if  $D = 3.2$  kpc.

## 5 SUMMARY AND CONCLUSIONS

Radio interferometer observations are an important instrument in the characterisation of Galactic circumstellar envelopes. Not only they permit us to reliably trace the ionized medium surrounding an evolved star, but also to derive different physical parameters of these objects.

However, the synthesis imaging process from interferometer data is optimised for point source observations. When extended sources are to be imaged we found that different algorithms, like the multi-scale CLEAN, give more satisfactory results in terms of image quality. For sources extended more than the interferometer LAS we also complemented the interferometer data with single-dish maps in order to get to a qualitatively and quantitatively reliable representation of the sky.

The combination process, via feathering, resulted fundamental for the two SNRs, for which the mere VLA maps were extremely poor and the recovered flux density was a factor 3 or 4 less than the real one. The information availability in a very wide range of spatial frequencies allowed us to create accurate and detailed images of these objects. Furthermore, the two SNRs served as a test to verify that this simple procedure can be used to perform also quantitative analyses on very extended sources.

For this reason we used SNR G011.2-00.3 mainly to test the method, and in particular the total flux density recovery. This source, in fact, has been deeply studied so far and a good base knowledge is available in literature. What we found is a perfect agreement between our flux density determination and the literature estimates from single-dish data. The resulting map at 5 GHz is currently the best representation of the source at this frequency.

For SNR G027.4+00.0 we were able to obtain important results. Using the 1.4-GHz map we posed a more stringent upper limit for the flux density of its yet non-detected pulsar. We did also show that the nebula presents a spatial variation of its radio spectral index. One hypothesis is that the flatter spectral index characterising the western region may be due to inhomogeneities of the strong magnetic field from the central object, causing a superposition of different ‘regular’ synchrotron contributions with different turnover frequencies. This, in turn, results in a global flatter spectrum. Alternatively it is also possible that the spectrum flattening could be ascribed to the impact of the SN shock on dense molecular clouds.

The possibility to accurately measure the flux densities also allowed us to constraint some physical parameters for the four PNe. In particular we were able to determine their ionized masses and their statistical distance. We found that all the four PNe have an ionized mass of order of  $0.1 M_{\odot}$ . For two of them it is possible to find in literature ionized mass estimates, via  $H\alpha$  or  $H\beta$  fluxes, that are in agreement with our results from radio. For the other two, as far as we know, our values are the first estimates.

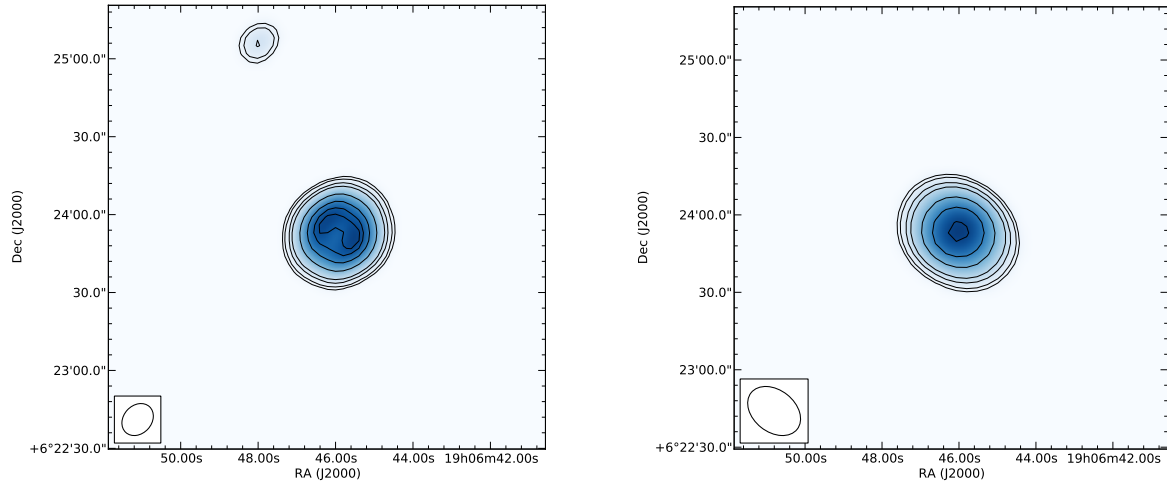


**Figure 10.** VLA image of PN G040-00.4 at 1.4 GHz (left) and 5 GHz (right).

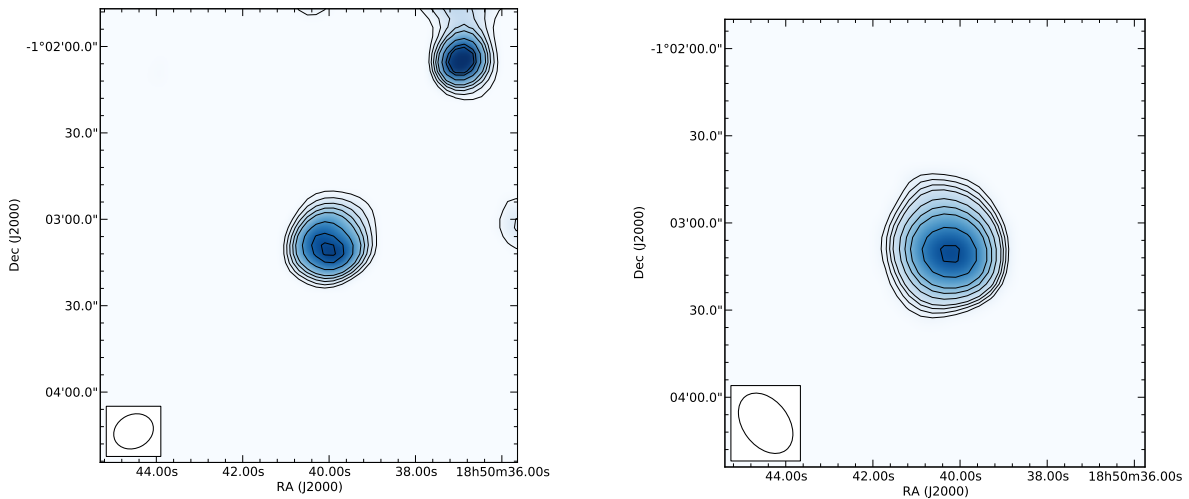


**Figure 11.** VLA image of PN G031.9-00.3 at 1.4 GHz (left) and 5 GHz (right).

We remark that this work has shown the importance of reliable radio data in multiwavelength studies. In fact radio maps can be successfully used to derive important physical parameters for different types of Galactic sources, regardless of their angular extensions. Eventually we want to stress that the procedure adopted for interferometer and single-dish data combination does not depend on the particular instruments used (VLA and GBT), since it works directly on FITS images. Therefore, given the positive results showed in this work, it can be applied as it is to different other interferometers such as ALMA, where flux-loss issues are even more important, and, in future, SKA.

#### ACKNOWLEDGEMENTS

This work is based on observations made with the Very Large Array and the Green Bank Telescope of the National Radio Astronomy Observatory, a facility of the National Science Foundation operated under cooperative agreement by Associated Universities

Inc.. Archive search made use of the SIMBAD database and the Vizier catalogue access tool, operated by the Centre de Données astronomique de Strasbourg.

#### REFERENCES

- Abell G. O., 1955, *PASP*, 67, 25
- Abell G. O., 1966, *ApJ*, 144, 259
- Altenhoff W. J., Downes D., Goad L., Maxwell A., Rinehart R., 1970, *A&AS*, 1, 319
- Angerhofer P. E., Becker R. H., Kundu M. R., 1977, *A&A*, 55, 11
- Bhatnagar S., Rau U., Green D. A., Rupen M. P., 2011, *ApJ*, 739, L20
- Becker R. H., Kundu M. R., 1975, *AJ*, 80, 679
- Cahn J. H., Kaler J. B., 1971, *ApJS*, 22, 319
- Cahn J. H., Rubin R. H., 1974, *AJ*, 79, 128
- Cahn J. H., Kaler J. B., Stanghellini L., 1992, *A&AS*, 94, 399
- Carey S. J., et al., 2009, *PASP*, 121, 76

- Caswell J. L., Haynes R. F., Milne D. K., Wellington K. J., 1982, *MNRAS*, 200, 1143
- Clark B. G., 1980, *A&A*, 89, 377
- Clark B. G., 1999, in Taylor G. B., Carilli C. L., Perley R. A., eds, *ASP Conf. Ser. Vol. 180, Synthesis imaging in radio astronomy II*. Astron. Soc. Pac., San Francisco, p. 1 Scappini F., Caselli P., Attolini M. R., 1995, *MNRAS*, 276, 57
- Condon J. J., Kaplan D. L., 1998, *ApJS*, 117, 361
- Condon J. J., Cotton W. D., Greisen E. W., Yin Q. F., Perley R. A., Taylor G. B., Broderick J. J., 1998, *AJ*, 115, 1693
- Cornwell T. J., 2008, *IEEE Journal of Selected Topics in Signal Processing*, Vol. 2, Issue 5, p.793-801
- Curtis H. D., 1919, *PASP*, 31, 285
- Dickel J. R., Milne D. K., 1972, *AuJPh*, 25, 539
- Dobrinčić M., Villaver E., Guerrero M. A., Manchado A., 2008, *AJ*, 135, 2199
- Downes A., 1984, *MNRAS*, 210, 845
- Dreyer J. L. E., 1888, *MNRAS*, 49, 1
- Emerson D. T., Gräve R., 1988, *A&A*, 190, 353
- Frew D. J., Parker Q. A., 2010, *Publ. Astron. Soc. Aust.*, 27, 129
- Frew D. J., et al., 2014, *MNRAS*, 440, 1345
- Gaensler B. M., Slane P. O., 2006, *ARA&A*, 44, 17
- Giacani E., Smith M. J. S., Dubner G., Loiseau N., 2011, *A&A*, 531, A138
- Giammanco C., et al., 2011, *A&A*, 525, A58
- Glushak A. P., 2014, *ARep*, 58, 6
- Gorny S. K., Stasińska G., Tylenda R., 1997, *A&A*, 318, 256
- Gotthelf E. V., Vasisth G., 1997, *ApJ*, 486, L133
- Gotthelf E. V., Vasisth G., Dotani T., 1999, *ApJ*, 522, L49
- Gregory P. C., Taylor A. R., 1986, *AJ*, 92, 371
- Gregory P. C., Scott W. K., Douglas K., Condon J. J., 1996, *ApJS*, 103, 427
- Helfand D. J., Becker R. H., White R. L., Fallon A., Tuttle S., 2006, *AJ*, 131, 252
- Högbom J.A., 1974, *A&AS*, 15, 417
- Hromov G. S., Kohomek L., 1968, *BAICz*, 19, 1
- Ingallinera A., et al., 2014, *MNRAS*, 437, 3626
- Kaler J. B., 1983, *ApJ*, 271, 188
- Kassim N. E., 1988, *ApJS*, 68, 715
- Kassim N. E., 1989, *ApJ*, 347, 915
- Kriss G. A., Becker R. H., Helfand D. J., Canizares C. R., 1985, *ApJ*, 288, 703
- Koo B.-C., Heiles C., 1991, *ApJ*, 382, 204
- Koo B.-C., Moon D.-S., Lee H.-G., Lee J.-J., Matthews K., 2007, *ApJ*, 657, 308
- Kothes R., Reich W., 2001, *A&A*, 372, 627
- Kumar H. S., Safi-Harb S., 2010, *ApJ*, 725, L191
- Kumar H. S., Safi-Harb S., Slane P. O., Gotthelf E. V., 2014, *ApJ*, 781, 41
- Kwok S., Zhang Y., Koning N., Huang H.-H., Churchwell E., 2008, *ApJS*, 174, 426
- Large M. I., Mathewson D. S., Haslam C. G. T., 1961, *MNRAS*, 123, 123
- Lenzuni P., Natta A., Panagia N., 1989, *ApJ*, 345, 306
- Lin L., et al., 2011, *ApJ*, 740, L16
- Maciel W. J., 1984, *A&AS*, 55, 253
- McMullin J. P., Waters B., Schiebel D., Young W., Golap K., 2007, *ASPC*, 376, 127
- Milne D. K., 1969, *AuJPh*, 22, 613
- Milne D. K., 1979, *AuJPh*, 32, 83
- Milne D. K., Aller L. H., 1982, *A&AS*, 50, 209
- Mizuno D. R., et al., 2010, *AJ*, 139, 1542
- Morsi H. W., Reich W., 1987, *A&AS*, 71, 189
- O'dell C. R., 1962, *ApJ*, 135, 371
- Ortiz R., 2013, *A&A*, 560, A85
- Pazderska B. M., et al., 2009, *A&A*, 498, 463
- Phillips J. P., 2004, *MNRAS*, 353, 589
- Phillips J. P., Ramos-Larios G., 2008, *MNRAS*, 383, 1029
- Phillips J. P., Márquez-Lugo R. A., 2011, *RMxAA*, 47, 83
- Reynolds S. P., Lyutikov M., Blandford R. D., Seward F. D., 1994, *MNRAS*, 271, L1
- Rieke G. H., et al., 2004, *ApJS*, 154, 25
- Sabbadin F., 1986, *A&A*, 160, 31
- Sanbonmatsu K. Y., Helfand D. J., 1992, *AJ*, 104, 2189
- Shaver P. A., Goss W. M., 1970, *AuJPA*, 14, 77
- Stanghellini L., Corradi R. L. M., Schwarz H. E., 1993, *A&A*, 279, 521
- Stil J. M., et al., 2006, *AJ*, 132, 1158
- Tajitsu A., Tamura S., 1998, *AJ*, 115, 1989
- Taylor A. R., Gregory P. C., 1983, *AJ*, 88, 1784
- Taylor A. R., Goss W. M., Coleman P. H., van Leeuwen J., Wallace B. J., 1996, *ApJS*, 107, 239
- Tian W. W., Leahy D. A., 2008, *ApJ*, 677, 292
- Todt H., et al., 2013, *MNRAS*, 430, 2302
- Torii K., Tsunemi H., Dotani T., Mitsuda K., 1997, *ApJ*, 489, L145
- van de Steene G. C., Zijlstra A. A., 1995, *A&A*, 293, 541
- Vasisth G., Aoki T., Dotani T., Kulkarni S. R., Nagase F., 1996, *ApJ*, 456, L59
- Vasisth G., Gotthelf E. V., 1997, *ApJ*, 486, L129
- Wachter S., Mauerhan J. C., Van Dyk S. D., Hoard D. W., Kafka S., Morris P. W., 2010, *AJ*, 139, 2330
- Weinberger R., Sabbadin F., 1981, *A&A*, 100, 66
- White R. L., Becker R. H., Helfand D. J., 2005, *AJ*, 130, 586
- Wilson T. L., Rohlfs K., Huttemeister S., 2012, *Tools of Radio Astronomy*, fifth edition, Springer
- Zhang C. Y., 1995, *ApJS*, 98, 659
- Zijlstra A. A., Pottasch S. R., Bignell C., 1989, *A&AS*, 79, 329